

Contents lists available at ScienceDirect

Journal of the Mechanics and Physics of Solids

journal homepage: www.elsevier.com/locate/jmps



Sliding of adhesive nanoscale polymer contacts

Debashish Das*, Ioannis Chasiotis

Aerospace Engineering, University of Illinois at Urbana-Champaign, Urbana, IL



ARTICLE INFO

Article history: Received 23 October 2019 Revised 2 March 2020 Accepted 4 March 2020 Available online 9 March 2020

Keywords:
Interfacial shear strength
Van der Waals
Nanofibers
Adhesion
Friction
JKR
Maugis-Dugdale
linear elastic fracture mechanics
Shear yielding

ABSTRACT

The interaction between friction and adhesion is a defining factor of the macroscopic behavior of natural and synthetic soft materials. In this work, the interfacial normal and shear adhesion strength of contacts between nanoscale polymeric fibers were studied using novel experiments aided by micromachined devices by which the critical normal and tangential pull-off forces between individual polyacrylonitrile (PAN) nanofibers with diameters in the range 400 nm - 4 µm were measured in real-time. The work of adhesion under normal detachment, as computed using the Johnson-Kendall-Roberts (JKR) and the Maugis-Dugdale (M-D) models for elastic adhesive contact, was shown to be independent of the nanofiber diameter and comparable to twice the surface energy of bulk PAN. Under shear detachment, peeling of the contact area was calculated using the JKR and the M-D models combined with linear elastic fracture mechanics (LEFM). The M-D model combined with LEFM could predict the experimentally obtained tangential pull-off force instabilities. The interfacial shear adhesion strength is shown to be constant for a broad range of contact radii (25-140 nm) and approximately equal to the material shear stress at yielding. Thus, shear yielding is shown to be the controlling mechanism during shear detachment of individual polymer nanofibers interacting with strong van der Waals adhesion.

© 2020 Elsevier Ltd. All rights reserved.

1. Introduction

Networks of interconnected filaments are ubiquitous in biological and bioengineered systems, such as connective tissues, extracellular matrix, spider webs, scaffolds for tissue growth and regeneration, as well as consumer products, such as personal care and hygiene products, energy devices, filtration systems, protective clothing, paper, etc. (Ramakrishna et al., 2006; Wang et al., 2013; Qin et al., 2015; Liang et al., 2010; Dong et al., 2011). The mechanical response and microstructural evolution of such networks under load are determined by the elastic-to-interfacial ratio of the stored energy, its spatial distribution, and the interaction between the two energy forms. For example, it was recently shown that in spider silk (Guo et al., 2018), the synergistic interplay between glue adhesion, stiffness of the silk and possibly of the web-network, and the strength of the silk strands leads to superior adhesion, energy absorption, and structural robustness of the web. It is the enhanced performance of the web that enables a spider to catch its prey, in contrast to the common view that the glue adhesiveness alone determines the efficacy of the web. While at the macroscale, the majority of the energy stored in a fiber network is in the form of elastic strain energy because of bending and stretching of individual fiber segments, nanoscale systems under load are characterized by a dynamic redistribution of elastic strain energy and a significant fraction of in-

E-mail addresses: ddas5@illinois.edu, debritum@gmail.com (D. Das), chasioti@illinois.edu (I. Chasiotis).

^{*} Corresponding author.

terfacial energy due to adhesive contact between nanofibers. The geometrical/structural complexity of a nanofiber network and the lack of knowledge of the adhesive interactions between nanofibers, limit our ability to understand the mechanical and dissipative processes in nanofibrous biological systems and our capability to design networks with tailored properties, such as strength, ductility, and toughness. The dimensions and boundary conditions, mechanical properties, and van der Waals adhesion between nanofibers, as well as the density of a nanofiber network, are among the controlling factors of the macroscale mechanical behavior of such non-bonded networks and determine the kinematics and bundling of filaments (Bobaru, 2007; Picu and Sengab, 2018; Sengab and Picu, 2018; Vader et al., 2009).

Experimental studies of single nanofiber adhesion are scarce, mainly due to difficulties in manipulating individual nanofibers and the lack of proven tools with nanonewton force and displacement resolution. Very few such studies have been concerned with the work of adhesion through the normal detachment of two nanofibers in crossed-cylinder (Shi et al., 2010, 2012; Wang et al., 2012; Stachewicz et al., 2014; Wang et al., 2017) and in parallel-cylinder (Stachewicz et al., 2014) configurations, not addressing the process of sliding, which is common in planar fiber networks in which both tangential and normal tractions are transmitted across a contact interface. An earlier study by Autumn et al. (2000) reported the sliding forces as a function of normal preload of a single gecko seta comprised of hundreds of 200–500 nm wide spatula-shaped structures on micromachined force sensors. While the study concluded that adhesion is due to intermolecular van der Waals forces, no sliding experiments were possible at the level of individual filaments comprising the nanostructured spatulae.

This study focuses on the sliding motion between two polymeric nanofibers, which can be treated as a 'single asperity' interfacial friction process. Soft materials such as polymers can conform elastically to small surface irregularities, and thus, a nearly perfect contact may be attained between two polymer surfaces, leading to higher adhesion/friction forces when compared to stiff elastic solids (Fuller and Tabor, 1975). Importantly, because adhesion is dominant, there is always friction even under zero or tensile external normal forces, and as such, single asperity interfacial friction is quite different from conventional friction observed between rough surfaces at the macroscale (Homola et al., 1990). Under single asperity interfacial friction, the frictional forces are proportional to the contact area resulting in a critical shear stress. In conventional friction, on the other hand, the frictional force is proportional to the normal force (not the contact area), and its magnitude is generally lower than that of interfacial friction at small normal forces (Homola et al., 1990).

Hence, knowledge of the contact area is essential in interfacial friction. Some studies have attempted to use a combination of linear elastic fracture mechanics and contact mechanics to estimate the area of contact, which is a critical parameter giving rise to interfacial friction, and also explain experimental observations in macroscale contacts: Saykoor and Briggs (1977) extended the Johnson-Kendall-Roberts (JKR) solution (mode I) (Johnson et al., 1971) to tangential forces (mode II/mode III) for the adhesive contact between two smooth elastic spheres. They assumed a singular stress field in the tangential direction and combined the strain energy release rates to obtain the solution to the mixed-mode problem. However, they did not account for frictional energy dissipation as the contact evolved, and assumed that the critical energy release rate remains equal to the work of adhesion. This led to an overestimate of the reduction of the contact area with increasing tangential force. Johnson (1996) was the first to reconsider Savkoor's and Briggs' model (Savkoor and Briggs, 1977) to account for the mode-mixity-dependent work of adhesion, by using an empirical function to tune the interaction between modes. A follow-up model (Johnson, 1997) allowed for frictional energy dissipation and microslip expanding from the periphery into the contact area. Johnson introduced cohesive zones to eliminate singularities in both normal (through the M-D model) and tangential traction distributions. Waters and Guduru (2009) performed experiments on the adhesive contact of a glass sphere on a planar PDMS surface and found that a mixed-mode model such as that introduced by Hutchinson and Suo (1991) could predict well the decrease in the contact area with increasing tangential force, at least until the initial peeling regime when circular symmetry was still maintained. The authors also observed that after a phase of symmetric peeling, the contact area under a compressive normal force became asymmetric with significantly more peeling occurring at the trailing edge of the contact compared to the leading edge. Under a tensile normal force, however, the contact area remained symmetric and circular until separation. Waters and Guduru restricted their analysis to the symmetric peeling phase. The contact area reduction under shear was as much as 60% and 40% for compressive and tensile normal forces, respectively. Recently, Papangelo and Ciavarella (2019) adopted a different mode-mixity function from Hutchinson (1990) (also in Hutchinson and Suo (1991)) to explain the experimentally observed decrease in the contact area with increasing tangential force and the locus of the jump instability points observed by Mergel et al. (2018). Recent compression-shear contact experiments with macroscale elastomers by Sahli et al. (2018) showed that both the apparent and the real contact area for smooth (single asperity) and rough (multiple asperity) contacts, respectively, decrease by as much as 30%. The initial smooth circular single asperity contact becomes an asymmetric ellipse under increasing shear force. However, the quadratic decay of the contact area, as observed experimentally, remains unchanged during the cross-over to asymmetric peeling.

Despite the significant advances in theoretical and experimental understanding of the mechanics of adhesive contacts subjected to tangential forces, there remains a lot to explore: Macroscale experiments (Mergel et al., 2018; Sahli et al., 2018) have shown that for an increasing tangential force, peeling of the contact leads to a reduction of the contact area, while sliding commences when the tangential force becomes equal to the product of the interfacial shear strength and the reduced contact area. However, after sliding commences, a wide range of behaviors for elastomers have been reported, including steady-state sliding (Varenberg et al., 2006; Vaenkatesan et al., 2006), instabilities and reattachment folds leading

the contact (Rand and Crosby, 2006), and instabilities trailing the contact (Waters and Guduru, 2009; Shen et al., 2008). Theoretically, it becomes quite challenging to predict the contact sliding initiation and subsequent evolution, which is further complicated by the extreme sensitivity to the form of the selected mixed-mode function and the model parameters (Papangelo and Ciavarella, 2019).

While these questions are still open topics of discussion for macroscale contacts, there is even less available knowledge about the process of sliding of contacts at the micrometer and nanometer length scales. Prior experimental studies utilized a surface force apparatus (SFA) (Israelachvili and Tabor, 1972; Homola et al., 1989; Homola et al., 1990; Maeda et al., 2002), a mesoscale friction tester (MFT) (Wang et al., 2007; Xu et al., 2007), and an atomic force microscope (AFM) (Carpick et al., 1996; Sheehan and Lieber, 1996; Carpick and Salmeron, 1997; Dietzel et al., 2008) to carry out fundamental studies of adhesion and friction at the micro/nanoscale. These studies, mainly focusing on hard materials, e.g. mica on mica (Homola et al., 1990; Homola et al., 1989), Pt on mica (Carpick et al., 1996), and MoO₃ nanocrystals on MoS₂ surfaces (Sheehan and Lieber, 1996), have shown that at small normal forces, the interfacial friction force is directly proportional to the contact area. However, studies on interfacial friction between micro/nanoscale polymer contacts remain scarce, Maeda et al. (2002) studied the contact of polystyrene and polyvinyl benzyl chloride films coated on mica surfaces to show that the state of polymer chains (degree of crosslinking, density of free long chains, and density of free ends of chains) determines the friction force which, in turn, correlates with the adhesion hysteresis. Yet, many important questions remain unanswered in micro/nanoscale polymer tribology, such as, whether the interfacial friction force is proportional to the contact area, what is the critical condition for the onset of sliding, and, importantly, how adhesion and friction are related to one another. Answers to such fundamental questions could serve as the underpinnings in computational modeling of the deformation of micro and nanofiber polymer networks. However, to the best knowledge of the authors, there are no prior studies on the sliding between nanoscale polymer fibers. This study addresses for the first time the combined normal and shear contact force interaction arising from van der Waals forces between individual polymeric nanofibers via a novel experimental method that provides simultaneous and independent measurements of the normal and tangential forces during the sliding process of freestanding nanofibers. A theoretical framework using the JKR and the Maugis-Dugdale (M-D) (Maugis, 1992) models combined with linear elastic fracture mechanics (LEFM) provides predictions for the peeling of the contact area, and the critical interfacial shear stress at detachment.

2. Materials and methods

Polyacrylonitrile (PAN) nanofibers were selected as the test material for this study, because they deform homogeneously without strain localization and necking during uniaxial tension (M. Naraghi et al., 2007a), which simplifies the interpretation of our measurements. Electrospinning of PAN nanofibers was carried in a custom-built electrospinning chamber with 9, 12, and 15 wt.% solutions of PAN powder with molecular weight 150,000 g/mol, in N,N-dimethylformamide (Sigma–Aldrich), at room temperature and through constant stirring for 24 hr. The electrospinning voltage and the distance to the collector were 25 kV and 25 cm (Naraghi et al., 2011), respectively, at a relative humidity of 17% that was maintained using calcium sulfate desiccant. PAN nanofibers were deposited in a suspended form on a wireframe collector and subsequently were annealed at 105° C (T_g+20° C) for 2 h ($T_g=85^{\circ}$ C, as reported by the manufacturer) to produce fibers with a very smooth surface, e.g. Fig. 1(a-c). The fiber diameter was controlled by the polymer solution concentration: higher concentrations increase the solution viscosity, which in turn, limits the stretching effect of the electrostatic forces, hence resulting in thicker fibers.

Measurements of the adhesion between individual PAN nanofibers were made using Microelectromechanical System (MEMS)-based devices designed for nanomechanical experiments. All experiments were conducted in ambient conditions (23 °C and 20-50% relative humidity) under an optical microscope to record high magnification optical images during testing. Digital image correlation (DIC) was applied to the optical images to calculate the relative motion of different components of the MEMS devices and thus derive the applied force on the fibers (Naraghi et al., 2010; M. Naraghi et al., 2007) with a resolution of ~2 nN. For each normal detachment test, two PAN fiber segments were isolated from the same fiber using a micromanipulator: one segment was mounted across a 50 µm section of the MEMS device, Fig. 1(d), and the other was mounted across two glass beads using a two-part epoxy, Fig. 1(e). Using fibers with the same diameter ensures a circular instead of an elliptical contact area for which only approximate solutions exist (Johnson and Greenwood, 2005). Fig. 1(f) shows a schematic of the normal detachment testing procedure, where the midpoints of two orthogonal fibers were first brought to contact, leading to an adhesive contact, and then were detached. Note that the midpoints of the fibers were chosen to remove any moments arising from the resultant tension components in the fibers. For a shear detachment test, two PAN fibers were fixed onto two MEMS devices and brought to contact by translation along the y-axis using a piezoelectric actuator, Fig. 1(g). The experimental apparatus allowed for the application of different normal forces, compressive or tensile, to the adhesive contact. The fibers were then detached in shear mode by translating the top MEMS device along the x-axis using a second piezoelectric actuator. The shear detachment apparatus was also used for midpoint normal detachment tests by restricting the translation of the top MEMS device along the y-axis. Each MEMS device was monitored by a dedicated high-resolution optical microscope/CCD camera system. After testing was completed, the fiber diameter was precisely measured via a Scanning Electron Microscope (SEM), Fig. 1(a-c).

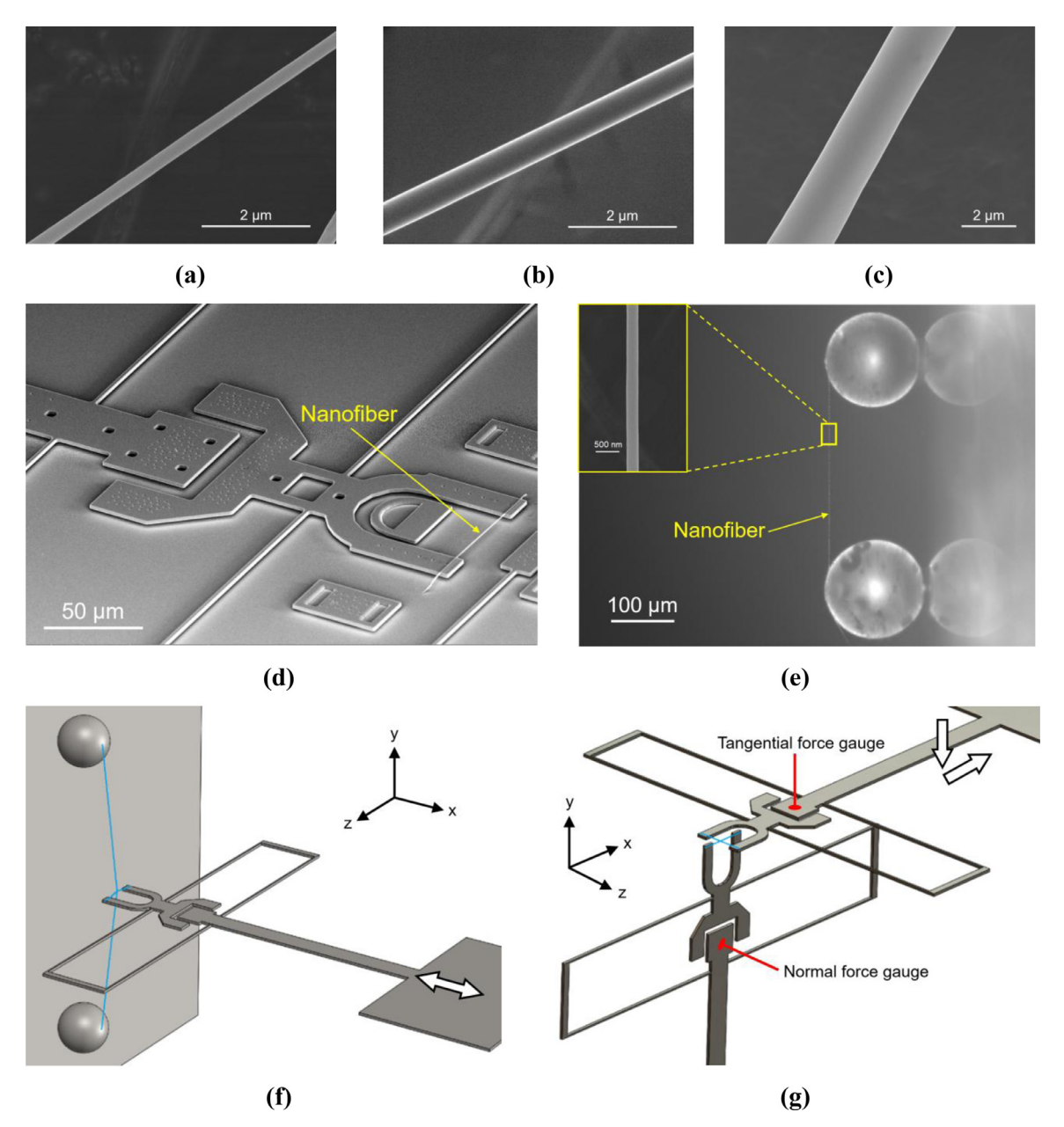


Fig. 1. Annealed electrospun PAN fibers from polymer solutions with polymer concentrations (a) 9 wt.%, (b) 12 wt.%, and (c) 15 wt.%. Annealing resulting in very smooth fiber surfaces. (d) Nanofiber mounted onto a MEMS device. (e) Nanofiber mounted between two glass beads. Inset: SEM micrograph of the PAN nanofiber, showing the uniform diameter along its length. (f) Schematic of the normal detachment test: two fibers are brought into adhesive contact in crossed-cylinder geometry, and subsequently pulled apart, (g) Schematic of the shear detachment test. In (f) and (g) the fibers are shown in blue color. (For interpretation of the references to colour in this figure legend, the reader is referred to the web version of this article.)

3. Results and discussion

3.1. Normal detachment

Fig. 2(a) shows a typical loading-unloading trajectory during a normal detachment test at a constant crosshead speed of 12 nms⁻¹. A snap-in instability, taking place when the effective spring constant of the force sensor becomes equal to the gradient of the true force-distance curve, can be observed in the force-displacement data as the fibers are brought close to each other. Further compression bends and stretches the fibers until a target compressive preload is reached, and then the fibers are unloaded. During unloading, the fibers detach when a tensile pull-off force is reached, which can be converted to

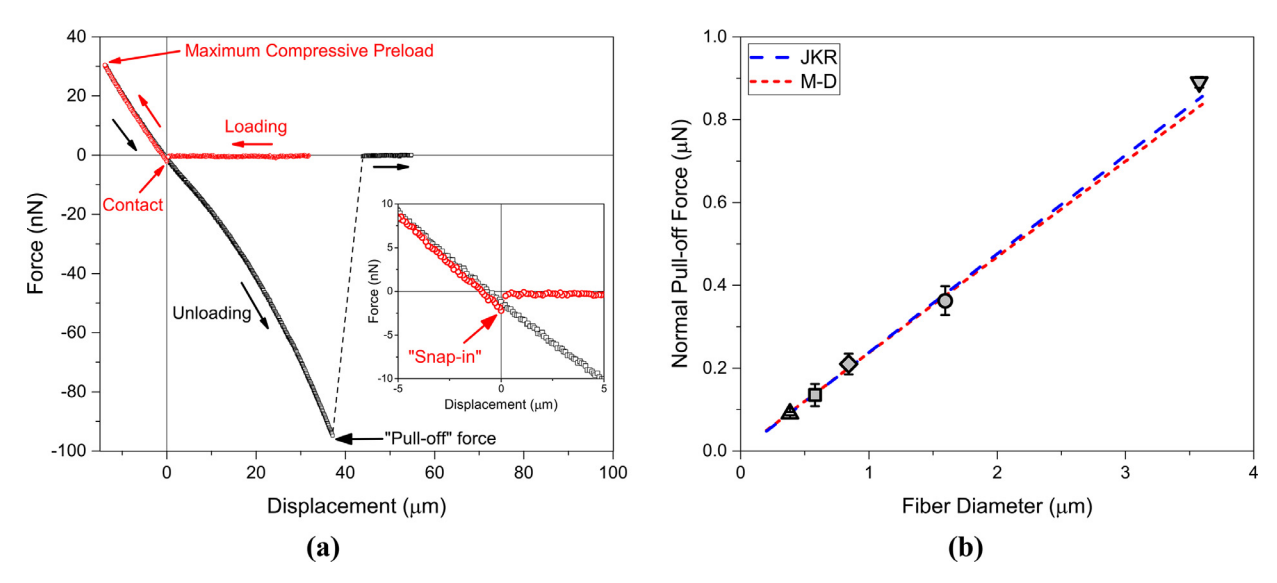


Fig. 2. (a) Force vs. displacement in normal detachment mode showing the pull-off force and the snap-in force (inset). The force-displacement curves were obtained at a cross-head speed of 12 nms⁻¹. (b) Pull-off force vs. fiber diameter. The force increases linearly with fiber diameter, as expected.

the work of adhesion (cohesion), w, via

$$F_{pull-off} = -\phi \pi R w \tag{1}$$

where $R=\sqrt{R_1R_2}$ is the effective contact radius for two cylinders with radii R_1 and R_2 in crossed configuration, and the parameter ϕ lies between 1.5 (JRK) (Johnson et al., 1971) and 2 (DMT) (Derjaguin et al., 1975). The JKR and DMT models that are used to describe the adhesion between two bodies in elastic contact represent extreme cases of contact as determined by Tabor's non-dimensional parameter, $\mu=(Rw^2/(E^{*2}z_0^3))^{1/3}$, where $E^*=[(1-\nu_1^2)/E_1+(1-\nu_2^2)/E_2]^{-1}$ and z_0 are the reduced elastic modulus and the equilibrium distance between the two surfaces in contact, respectively. For small values of Tabor's parameter, $\mu<0.1$, the DMT model is valid and works well for hard solids with negligible elastic deformation, while for larger values of the Tabor parameter, $\mu>5$, the JKR model is valid, and works well for soft adhering solids with large elastic deformation. Between these two extreme cases, a useful analysis in closed form was put forward by Maugis (1992), using the Dugdale approximation, where the adhesive stress σ_0 assumes a constant value until a critical separation h_0 between two surfaces is reached and the force interaction drops to zero. In the Maugis-Dugdale (M-D) model, the value of the critical separation is $h_0=(9\sqrt{3}/16)z_0\approx0.97z_0$. This value satisfies the condition that the work of adhesion w (with maximum force per unit area equal to σ_0) becomes equal to the interaction energy due to the Lennard-Jones potential in the adhesion region.

For the PAN nanofibers at hand, the Tabor parameter lies between: 5–12 (for 200 nm $\leq R \leq 2 \mu \text{m}$, $w = 100 \text{ mJ/m}^2$, and $z_0 = 0.165$ nm (Wang et al., 2017; Israelachvili, 2011)). In this first estimate, the value of w was chosen as twice the surface energy, γ , reported in literature ($\gamma = 50 \text{ mJ/m}^2$ (Wu, 1982), $\gamma = 49.9 \text{ mJ/m}^2$ (Pritykin, 1986)). Thus, the JKR theory is the appropriate model to describe the contact between two PAN nanofibers. However, the aforementioned value of z_0 was originally determined for a closed packed solid and prior studies have adopted a value of $z_0 = 1$ nm (Shi et al., 2010; Wang et al., 2012; Stachewicz et al., 2014) for the contact between polymer fibers, which is equivalent to the radius of gyration in a poor solvent, $R_g \sim 1$ nm for PAN ($M_w = 150,000$ g/mol). For $z_0 = 1$ nm, μ lies between 0.9–1.9, which requires the use of the Maugis-Dugdale (M-D) model. A comparison of the work of adhesion computed by the two models can be obtained using a plot of the pull-off force vs. fiber diameter, Fig. 2(b). Using the JKR model, the work of adhesion for PAN is found to be equal to $101\pm11 \text{ m}]/\text{m}^2$. In the M-D model ϕ (Eq. (1)) depends on the fiber diameter: Using an iterative scheme, the M-D value of the work of adhesion is computed as 96 ± 11 mJ/m², which is very close to the JKR model result and in good agreement with values reported in the literature for bulk PAN (Wu, 1982; Pritykin, 1986; Li et al., 2001). For the interacting PAN fibers, the strength and range of the normal interaction can be extracted using the M-D analysis. For $z_0 = 1$ nm, we find $h_0 \approx 0.97z_0 \approx 0.97$ nm, and therefore $\sigma_0 = w/h_0 \approx 100$ MPa. A strong van der Waals interaction is characterized by ~100 MPa strength and an interaction range of a few nanometers, consistently with the interaction parameters established for the PAN nanofibers in this work.

Finally, it is noted that the measured values of the work of adhesion were the same for relative humidity in the range 20–50%, which attests to the hydrophobic nature of PAN nanofibers (Feng et al., 2002).

3.2. Shear detachment

Fig. 3(a) shows the top view of a transverse sliding experiment, with the DIC-derived rigid body u displacements of two components of the MEMS force sensor superposed directly onto the image. The relative displacement of these two

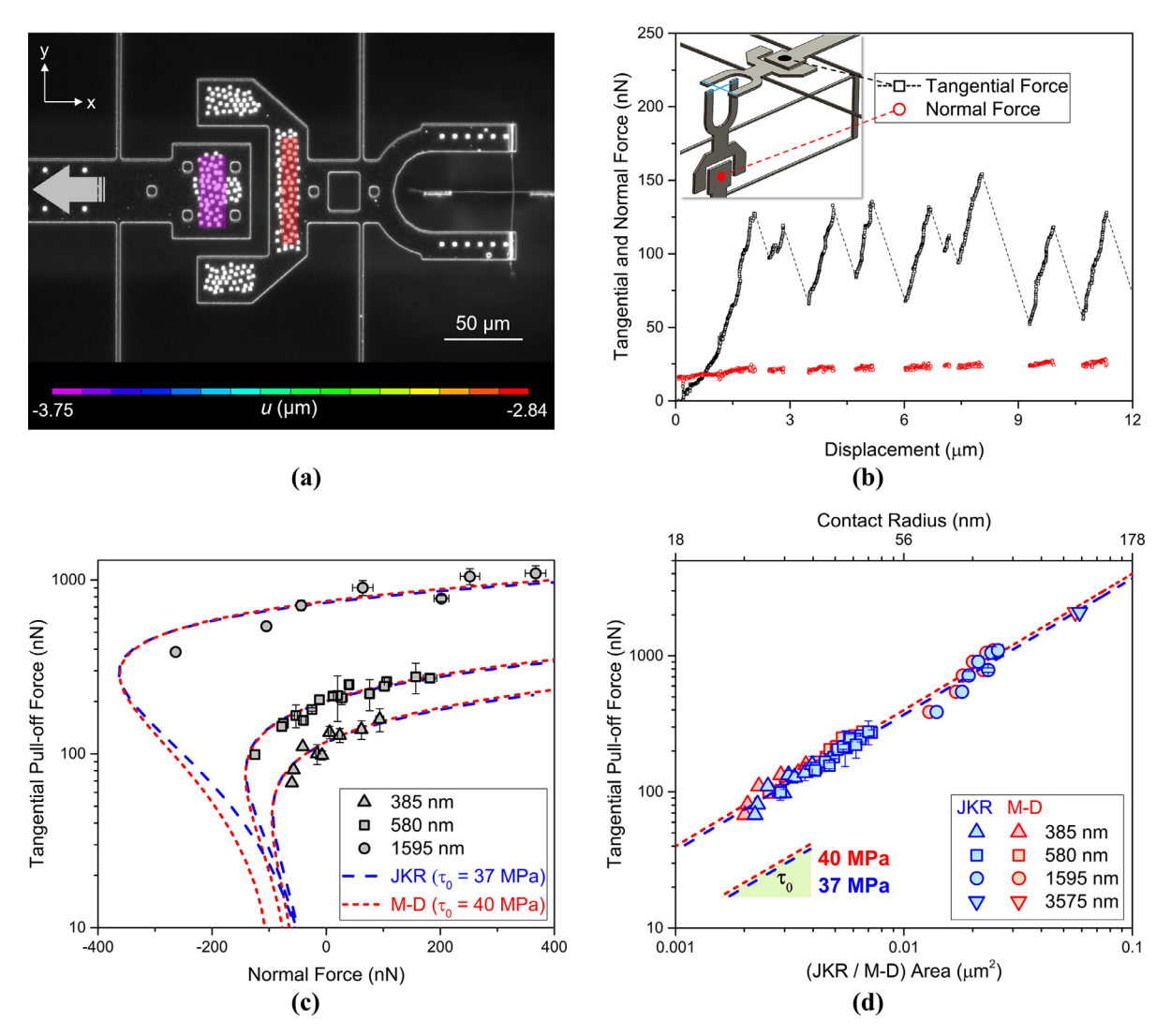


Fig. 3. (a) Top view of a portion of the MEMS testing device also showing the two crossed fibers (right) in a transverse sliding experiment. The rigid body u-displacements of two components of the MEMS device, as calculated via DIC, are superposed onto the image. (b) Tangential and normal force vs. displacement in shear detachment mode showing stick-slip behavior. The tests were done at a cross-head speed of 12 nms⁻¹. (c) Average tangential pull-off force vs. normal force in agreement with the JKR and M-D model predictions for 385 nm, 580 nm, and 1595 nm diameter fibers. The tangential pull-off forces for the two models were computed by multiplying the calculated contact areas by a constant critical shear stress. (d) Tangential pull-off force vs. contact area for a broad range of contact radii (25–140 nm). The constant of proportionality is the critical shear stress, $τ_0$, sustained by the PAN surfaces just before slip occurs. The constant $τ_0$ for a wide range of contact radii, using either the JKR or the M-D model, implies a potential correlation between $τ_0$ and a material property.

device components, multiplied by the spring constant of the device, provides the tangential force applied during transverse sliding. Under compressive normal forces, two PAN nanofibers exhibited a stick-slip behavior, Fig. 3(b), whereas under tensile normal forces, there was a single detachment event during sliding. The peak force in the stick phase was relatively constant, Fig. 3(b), and the critical tangential pull-off force, computed as the average of the peak stick forces, is reported here. The large displacements observed during the slip instabilities are due to the compliance of the test system, unlike in the AFM-based sliding experiments where the cantilever tip slips laterally to its most compliant mode (Carpick et al., 1996).

The effect of tangential forces on the evolution of an adhesive contact is quite complex and has been studied in some detail using continuum fracture mechanics concepts (Johnson, 1996; Johnson, 1997; Waters and Guduru, 2009; Papangelo and Ciavarella, 2019). When tangential forces are applied to an adhesive contact, there is an interaction between adhesion and friction and the effective adhesion is reduced, hence decreasing the contact size. Experiments with dry sliding of mica on mica (Israelachvili and Tabor, 1972; Homola et al., 1990), platinum on mica (Carpick et al., 1996), and tungsten on mica (Xu et al., 2008) have revealed that the tangential pull-off force is directly proportional to the contact area and thus, the frictional shear stress is constant and independent of the normal force. Thus, for low amplitude normal forces, when adhe-

sion dominates, the tangential force at detachment is described by

$$T_c = \tau_0 A \tag{2}$$

where τ_0 is the critical shear stress at pull-off, and A is the area of the contact at the peak tangential force, which is smaller than the contact area established just due to the normal force. However, Homola et al. (1989) did not observe a change in the contact area from that predicted by the JKR model for normal contact, after a tangential force was applied. Similarly, Carpick et al. (1996) showed a proportional relationship between the tangential friction force and the contact area calculated using the JKR model for normal contact only. Johnson (1997) showed that the contact areas in the experimental work by Carpick and Homola et al. were reduced by only a few percent, which may explain why they were reported to be independent of the tangential force.

While the aforementioned microscale contact studies focused on crystalline and hard materials (Homola et al., 1989: Carpick and Salmeron, 1997), herein we find that, for polymers too, the critical tangential pull-off force is approximately proportional to the JKR or the M-D contact areas for different normal forces and fiber diameters. Fig. 3(c) shows the experimental data obtained for three fiber diameters vs. the predictions obtained by multiplying the IKR and the M-D calculated contact areas with a constant critical shear stress value of 37 MPa, and 40 MPa, respectively. Prior research on micro/macroscale polymers has shown that the contact area varies with the normal force according to the JKR contact model (Sahli et al., 2018; Maeda et al., 2002), and the macroscale frictional force is proportional to the observed contact area (Shooter and Tabor, 1952). Herein it is shown for the first time that for nanoscale polymer contacts too, the frictional/tangential pull-off force is proportional to the contact area predicted from the normal force using the JKR/M-D models for elastic adhesive contacts, as shown in Fig. 3(d). The critical shear stress of 37 MPa for the JKR model is the slope (37±4 MPa) of the blue dashed line in Fig. 3(d), obtained by linear fitting of the data of the tangential pull-off force vs the IKR contact area for all fiber diameters. For the M-D model, the contact radius was taken as b = a + 0.4(c - a) as given by Johnson, 1997, where a and c are the radius of the intimate contact and the radius to which the adhesive forces extend, respectively. A value of 40±4 MPa was obtained by using the M-D model. It should be noted that the critical tangential forces obtained from the 1595 nm diameter fiber did not fit very well either the JKR or the M-D curves for a constant shear stress value, Fig 3(c). A rather linear trend is demonstrated, which is similar to the findings by Waters and Guduru (2009) for the sliding of a macroscale spherical glass probe on a flat PDMS surface. This is attributed to the load-dependent term, μP (μ is the coefficient of friction) that becomes increasingly important with increasing contact size, in addition to the adhesive forces, to describe the total friction force $T = \tau_0 A + \mu P$ (Whitten and Brown, 2007). However, the mean critical shear stress values predicted via the JKR and the M-D models for the 1595 nm diameter fiber are essentially the same as those computed for the smaller diameter fibers but with a larger variance. Therefore, we will consider that the critical shear stress, τ_0 , sustained by two PAN surfaces, before an instability and macroslip occur, is approximately constant and equal to 37 ± 4 MPa (JKR) or 40±4 MPa (M-D) for a wide range of contact radii (25-140 nm), Fig. 3(d). Such high numbers for the critical shear stress are not uncommon in polymer friction studies: Whitten and Brown (2007) reported values of 19-39 MPa for glassy polymers. Notably, $\tau_0 \approx (1/30)G$, where $G = E/(2+2\nu) = 3/(2+0.7)$ GPa ≈ 1.1 GPa is the shear modulus of PAN, is also the theoretical shear strength of crystalline materials or the frictional stress of nanoscale commensurate contacts (Hurtado and Kim, 1999). However, the mechanism of friction in polymeric surfaces can be very different from that in crystalline materials (Maeda et al., 2002). The reason for the high tangential detachment (friction) forces, and consequently the high interfacial shear stresses, is the high polarity of PAN due to the presence of the nitrile group, which is the cause of substantial adhesion hysteresis (Li et al., 2001), and correlates with higher friction forces (Maeda et al., 2002).

Yet, the question still remains whether for polymer nanofibers, the JKR or M-D derived contact areas, due to normal forces only, are still applicable at the peak tangential force. Sahli et al. (2018) reported contact area reductions as large as 30% before the onset of sliding of a smooth glass sphere on a flat PDMS surface. Similarly, for the same type of contact, Waters and Guduru (2009) demonstrated stick-slip and contact area reduction at the peak tangential force, which was as large as 60% and 40% for compressive and tensile normal forces, respectively. Sahli et al. (2018) further showed that the reduction rate of the apparent contact area with respect to the tangential force scales with the Young's modulus as $\alpha_A \sim 1/(E^{0.65})$. This implies that the reduction of the contact area due to a tangential force is larger for compliant contacting bodies as also discussed in (Sahli et al., 2018). Thus, a moderate reduction in the contact area is also expected during frictional sliding between PAN nanofibers, hence, the contact area at the peak tangential force is overpredicted by the JKR and the M-D models, and the value of τ_0 is, therefore, underestimated. However, the nanoscale area of contact is not amenable to direct observations or measurements, and must be deduced through theoretical considerations. The following sections incorporate linear elastic fracture mechanics (LEFM) into the JKR and M-D models to treat the reduction in the contact area and its evolution with tangential force.

3.2.1. Prediction of contact area evolution with tangential force using a combined JKR and LEFM model

The solution for the contact problem between two elastic spheres with radii R_1 and R_2 in the presence of adhesion can be used to study the contact of two elastic cylinders in the crossed configuration by substituting the equivalent radius $R = [1/R_1 + 1/R_2]^{-1}$ of two elastic spheres in contact with the equivalent radius $R = \sqrt{R_1R_2}$ of two elastic cylinders with radii R_1 and R_2 . For $R = R_1 = R_2$, which is the case in the present study, the contact area is circular, and the problem is equivalent to the contact between two elastic spheres of equal radius 2R or between an elastic sphere of radius R and a flat elastic-half space. If $R_1 \neq R_2$ the contact area is elliptical.

In the classical JKR contact formulation, the contact interface is frictionless and the mode I stress intensity factor is (Waters and Guduru, 2009; Papangelo and Ciavarella, 2019):

$$K_{I} = \frac{P_{a}}{2a\sqrt{\pi a}} = \frac{P_{H} - P}{2a\sqrt{\pi a}} \tag{3}$$

where the total applied normal force, P can be thought of as being comprised of a Hertzian component, $P_H = 4E^*a^3/(3R)$, with a denoting the contact radius, and a component corresponding to the Boussinesq flat punch solution, P_a , which gives rise to a singularity at the contact edge.

In the absence of tangential tractions, fracture occurs when the strain energy release rate reaches a critical value, G_c which is equal to the work of adhesion, w:

$$G = \frac{K_{\rm I}^2}{2E^*} = \frac{P_a^2}{8\pi E^* a^3} = G_c = w \Rightarrow P_a = \sqrt{8\pi E^* a^3 w}$$
 (4)

The classic JKR solution relating the force and the contact radius can then be obtained:

$$P = P_H - P_a = \frac{4E^*a^3}{3R} - \sqrt{8\pi E^*a^3 w}$$
 (5)

which takes the normalized form:

$$\bar{P} = \bar{a}^3 - \sqrt{6\bar{a}^3} \tag{6a}$$

where

$$\bar{P} = \frac{P}{\pi Rw} \text{ and } \bar{a} = a \left(\frac{4E^*}{3\pi wR^2}\right)^{1/3}$$
 (6b)

If a tangential force, *T*, is applied in addition to the normal force, in the absence of slip at the interface, a singularity in the tangential traction distribution at the contact periphery gives rise to mode II and mode III stress intensity factors (Johnson, 1997):

$$K_{II(\theta)} = \frac{T}{2a\sqrt{\pi a}}\cos\theta \text{ and } K_{III(\theta)} = \frac{T}{2a\sqrt{\pi a}}\sin\theta$$
 (7)

where θ is the angle between the direction of the applied tangential force and the radius vector. The strain energy release rate in a mixed-mode problem can be expressed as:

$$G = \frac{1}{2E^*} \left[K_l^2 + K_{ll(\theta)}^2 + \frac{1}{1 - \nu} K_{ll(\theta)}^2 \right]$$
 (8)

Johnson (1997) averaged K_{II} and K_{III} around the periphery of the contact to eliminate the θ dependence, assuming that the toughness of mode III was twice that of mode II (Eq. (8) for $\nu = 0.5$). Papangelo and Ciavarella (2019) suggested that averaging should be performed by multiplying the mode III contribution by ½ since Johnson's assumption would not be valid for an axisymmetric contact. By this averaging approach, the strain energy release rate becomes:

$$G = \frac{1}{2E^*} \left[K_I^2 + K_{II}^2 \right] = \frac{1}{8\pi E^* a^3} \left[P_a^2 + T^2 \right] \tag{9}$$

where K_{II} in the direction of the tangential force is calculated by setting $\theta = 0^{\circ}$ in Eq. (7). As previously, fracture occurs at the critical strain energy release rate, G_c :

$$G = \frac{1}{8\pi F^* a^3} \left[P_a^2 + T^2 \right] = G_c \Rightarrow P_a = \sqrt{8\pi E^* a^3 G_c - T^2}$$
(10)

Now, we can modify the classic JKR equation to account for the tangential force in addition to the normal force, as:

$$P = P_H - P_a = \frac{4E^*a^3}{3R} - \sqrt{8\pi E^*a^3G_c - T^2}$$
(11)

The mixed-mode critical strain energy release rate, G_c , is typically more than the work of adhesion, w: Experiments have shown (Cao and Evans, 1989) an apparent increase in the material toughness under mixed-mode loading. Such an increase in the macroscopic toughness is due to various microscopic processes such as plasticity, friction, etc. at the process zone near the crack tip. Phenomenological models have been proposed by Hutchinson and Suo, (1991) to explain this effect in bi-material interfaces, in which G_c depends on the degree of the mode-mixity, ψ :

$$G_c = wf(\psi) \text{ where } \psi = \tan^{-1}\left(\frac{K_{II}}{K_I}\right) = \tan^{-1}\left(\frac{T}{P_a}\right) = \tan^{-1}\left(\frac{T}{\bar{a}^3 - \bar{P}}\right)$$
(12)

where $\bar{T} = T/(\pi Rw)$ is the normalized tangential force.

Eq. (11) can now be written as:

$$P = \frac{4E^*a^3}{3R} - \sqrt{8\pi E^*a^3w \left(f(\psi) - \frac{T^2}{8\pi E^*a^3w}\right)} \Rightarrow P = \frac{4E^*a^3}{3R} - \sqrt{8\pi E^*a^3w'}$$
 (13a)

or

$$\bar{P} = \bar{a}^3 - \sqrt{6\bar{a}^3 X} \text{ where } X = \frac{w'}{w} = f(\psi) - \frac{T^2}{8\pi E^* a^3 w} = f(\psi) - \frac{\bar{T}^2}{6\bar{a}^3}$$
 (13b)

Thus, friction reduces the effective work of adhesion from w to w'. For given P, T, the contact area, a, can be predicted by Eq. (13), if the form of the mode-mixity function, $f(\psi)$, is known, which, in turn, controls the calculated contact area under increasing tangential force. To this effect, Savkoor and Briggs (1977) were the first to consider the interaction between adhesion and friction, although they assumed that the toughness of the contact interface remained constant with increasing tangential force, and hence the degree of mode mixity, implying that $f(\psi) = 1$. As a result of this assumption, their model underpredicted the area of contact and the critical tangential force at sliding. Subsequent studies (Johnson, 1996; Johnson, 1997; Waters and Guduru, 2009; Papangelo and Ciavarella, 2019) reconsidered Savkoor's and Briggs' model allowing for an increase in interfacial toughness with the degree of mode mixity, through empirical relations that were originally developed by Hutchinson and Suo (1991). Johnson (1996) was the first to adopt such an empirical relation to introduce mode-mixity dependence in contact formulations via an empirical constant, β :

$$f(\psi) = 1 + (1 - \beta)\tan^2\psi, (0 \le \beta \le 1)$$
(14a)

$$X = 1 + (1 - \beta) \left(\frac{\bar{T}}{\bar{a}^3 - \bar{p}}\right)^2 - \frac{\bar{T}^2}{6\bar{a}^3}$$
 (14b)

Later, Johnson (1997) extended this model to include cohesive zones for both mode I (as in the M-D model) and mode II via a rather arbitrary form of the mode-mixity function with a non-dimensional interaction factor, α :

$$f(g) = \sqrt{\left(1 + g\right)^2 - 2\alpha g} \tag{15a}$$

where

$$g = \frac{\tau_0 \overline{s}}{\sigma_0 h_0}, \ \overline{s} \le \overline{s}_0 \tag{15b}$$

and

$$g = \frac{\tau_0 \overline{s}_0}{\sigma_0 h_0}, \ \overline{s} > \ \overline{s}_0 \tag{15c}$$

In this model, the mode-mixity is introduced in terms of a local slip parameter, the mean slip displacement \bar{s} , which increases with increasing the far-field tangential force until a critical slip distance \bar{s}_0 is reached. Unlike other models, the tangential force does not influence the mode-mixity beyond \bar{s}_0 . This model captures the progression of microslip from the periphery to the interior of the contact area, and the jump instabilities with increasing tangential force in the combined M-D and LEFM treatment of the problem. However, such instabilities could not be captured by the combined JKR-LEFM formulation.

Waters and Guduru considered a different form of the mode-mixity function (Waters and Guduru, 2009; Hutchinson and Suo, 1991) to study the sliding contact of a glass sphere on a flat PDMS surface:

$$f(\psi) = 1 + \tan^2[(1 - \beta)\psi]$$
 (16a)

$$X = 1 + \tan^2 \left[(1 - \beta) \tan^{-1} \left(\frac{\bar{T}}{\bar{a}^3 - \bar{P}} \right) \right] - \frac{\bar{T}^2}{6\bar{a}^3}$$
 (16b)

This model could predict the evolution of the contact area with increasing tangential force as long as the contact remained circular.

Recently, Papangelo and Ciavarella (2019) considered the third form of the mode-mixity function proposed by Hutchinson and Suo (1991), which results in a simple relation between the interface toughness and the stress intensity factors:

$$f(\psi) = \left[1 + (\beta - 1)\sin^2\psi\right]^{-1}$$
 (17a)

$$\frac{1}{2F^*} \left[K_I^2 + \beta K_{II}^2 \right] = w \Rightarrow P_a = \sqrt{8\pi E^* a^3 w - \beta T^2} \Rightarrow \bar{P} = \bar{a}^3 - \sqrt{6\bar{a}^3 - \beta \bar{T}^2}$$
 (17b)

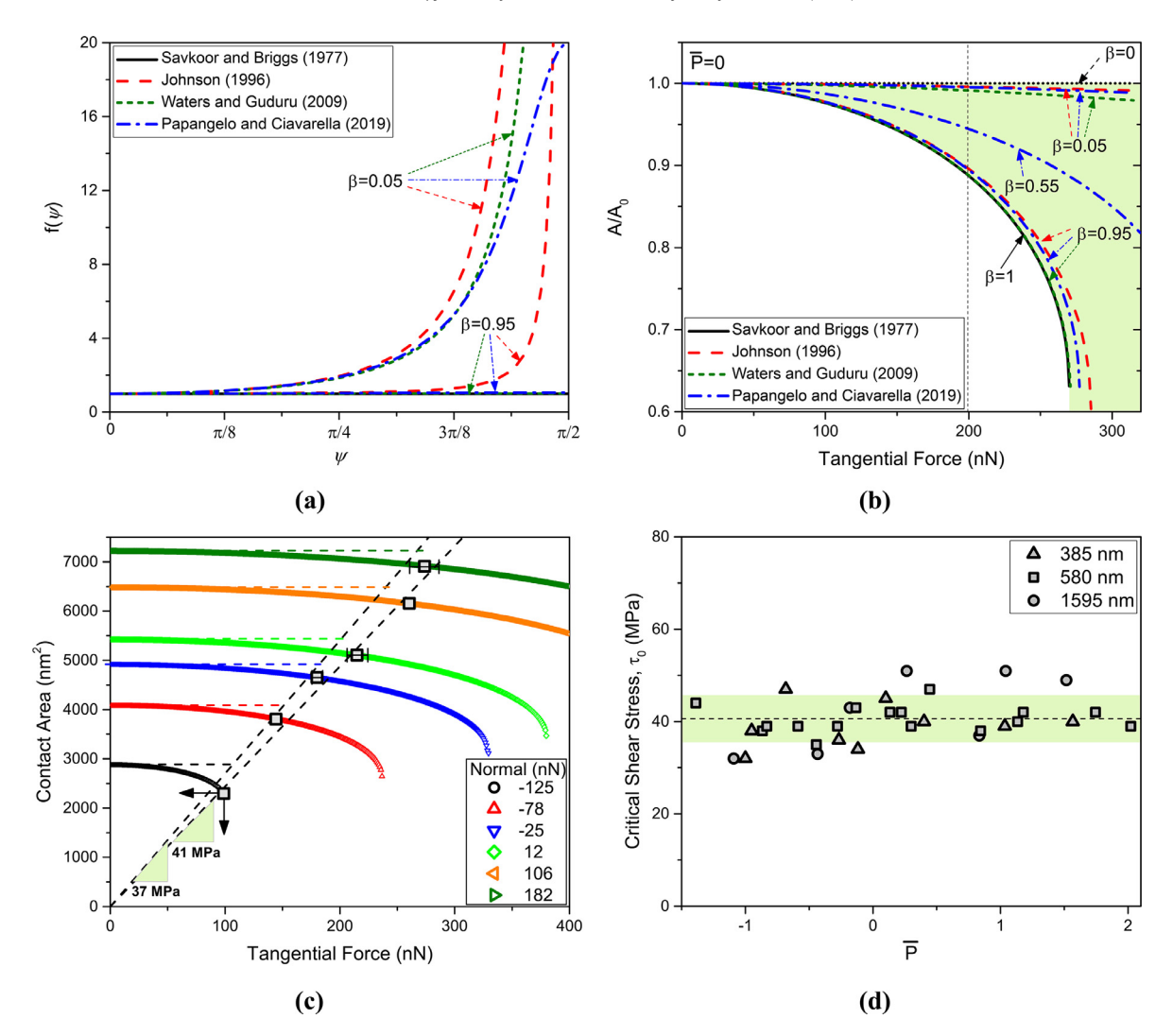


Fig. 4. (a) $f(\psi)$ for different values of the non-dimensional parameter β . $\beta=1$ represents a "brittle interface" with no increase in toughness, whereas $\beta=0$ represents the case of "mode uncoupling", with the tangential force not affecting the mode I problem. (b) Peeling of the contact area during the static phase predicted using various modified JKR models. The contact area reduction is maximum for $\beta=1$, and is unchanged for $\beta=0$. (c) Reduction of the contact area with increasing tangential force, T, for different values of the normal force and $\beta=0.55$. The square symbols correspond to the experimental T and T and T are indicated by the dashed line and the green highlight, respectively. (For interpretation of the references to colour in this figure legend, the reader is referred to the web version of this article.)

$$X = 1 - \beta \frac{\bar{T}^2}{6\bar{\sigma}^3} \tag{17c}$$

The solution to the problem formulated using this function $f(\psi)$ allows for instabilities to be captured under force or displacement control. Moreover, Papangelo and Ciavarella (2019) utilized all three mode-mixity functions reported in Hutchinson and Suo (1991) to show that the solution for the contact area is very sensitive to the form of $f(\psi)$. Notably, for β =1 Eqs. 14(a), 16(a), and 17(a) yield $f(\psi)$ = 1 for any value of T, which is the same as the Savkoor and Briggs model (Savkoor and Briggs, 1977), namely the interface behaves as "brittle", since the toughness does not increase with increasing mode mixity. This extreme case is pointed out in Fig. 4(a) for large values of β . At the other extreme, for β =0, Eq. 17(c) yields X = 1 and Eq. 13(b) reduces to Eq. 6(a), i.e. there is no effect of the tangential force on the adhesion process and thus, on the contact area. The same applies to Eqs. 14(b) and 16(b) and the contact area is independent of the tangential force as shown in Fig. 4(b). Thus, for β = 0, the two fracture modes are uncoupled, which, physically speaking, is not very realistic.

The aforementioned empirical forms of mode-mixity functions, $f(\psi)$, as described by Eqs. 14(a), 16(a), and 17(a), were applied to our experimental data to plot the contact area normalized by the initial area established due to normal forces only

(no tangential force), A/A_0 , as a function of the tangential force for the contact between two 580 nm diameter PAN fibers subjected to $\bar{P} = 0$, Fig. 4(b). The application of the mode-mixity function given by Eq. 15(a) is described in detail in the Supporting Information. The Young's modulus and Poisson's ratio of PAN are 3 GPa (Fig. 6) and 0.35, respectively, yielding $E^*=1.7$ GPa. The contact area reduction due to a tangential force is relatively insensitive to the mode-mixity function for small values of the tangential pull-off force applied in this study, Fig. 4(b). Therefore, the mode-mixity function used by Papangelo and Ciavarella is employed in the subsequent analyses since X is independent of \bar{P} , Eq. 17(c), which makes the problem more tractable in the M-D formulation. Considering all four models, in the case of no applied normal force, \bar{P} 0, the contact area reduction at the experimentally measured shear pull-off force $T \sim 200$ nN (represented by the dashed vertical line) can be as high as 11% for the full range of values for β , Fig. 4(b). However, at $\bar{P} = 0$, the model prediction for the lowest tangential force at the elastic jump instability (compliant system) is ~270 nN. The predicted critical tangential force at the elastic jump instability can be obtained as follows: At the limit value of $\beta=1$, Fig. 4(b), the rate of change of the contact area with the tangential force approaches infinity for $T \approx 270$ nN. In a force-controlled system, this would lead to a displacement jump. Also, as deduced from Fig. 4(b), the critical tangential force at the jump instability increases with decreasing β . Thus, the smallest value of the critical tangential force at the jump instability, $T \approx 270$ nN, is predicted for β =1. This value of T is still significantly higher than the experimental tangential pull-off force of 200 nN. Thus, sliding may initiate when a critical interfacial shear stress of the contact has been reached, which occurs at a lower value of T compared to the model predictions for an instability.

Therefore, it becomes clear that the value of β must be determined. For $\beta \approx 0$ there is no reduction in the contact area and the critical interfacial shear stress obtained in Fig. 3(d) would hold. If, however, $\beta \to 1$, then the contact area is reduced with a simultaneous increase in τ_0 . The corroborating information to determine an appropriate β is the value of T at which the sliding instability occurs. For instance, for a 580 nm fiber, $\beta = 0.55$ reproduced the sliding instability that was experimentally measured for T = 100 nN and P = -125 nN, Fig. 4(c). Also, for P = -125 nN, the model prediction for the tangential force at the jump instability was smaller than the experimental pull-off force for $\beta > 0.55$. Furthermore, for P > -125 nN, the combined JKR-LEFM model given by Eq. (17), could not predict the experimental jump instabilities for most of the experimental cases, even for the extreme case of $\beta = 1$. Therefore, $\beta = 0.55$ that has reproduced at least one of the experimentally observed sliding instabilities is considered in the discussion in this Section. The experimental mean tangential pull-off force (square symbols in Fig. 4(c)) divided by the corresponding contact area calculated by the model, provides the critical interfacial shear stress, τ_0 (as shown by the two black arrows in Fig. 4(c)). The experimental shear forces lie roughly on a straight line passing through the origin with the reciprocal of the slope giving $\tau_0 \approx 41$ MPa. The line drawn with a steeper slope ($\tau_0 \approx 37$ MPa) passing through the origin corresponds to $\beta = 0$ when there is no change in the contact area with increasing tangential force, as indicated by the dashed lines in Fig. 4(c) and Fig. 3(d).

The analysis in Fig. 4(c) for a PAN nanofiber with 585 nm diameter was extended to all the fiber diameters tested in this study. For $\beta=0.55$, the critical interfacial shear stress calculated from all mean experimental tangential pull-off forces and the corresponding contact areas is $\tau_0\approx41\pm5$ MPa. Remarkably, for all fiber diameters considered here and a broad range of compressive and tensile normal forces, τ_0 lies within a narrow band in Fig. 4(d).

An alternative treatment of the contact evolution with the applied tangential force was provided by Johnson's model (Johnson, 1997) who considered cohesive zones for both mode I and mode II components of the deformation. The details of the model and its application to the current polymer fibers are provided in the Supporting Information file, which could provide further understanding of the micromechanics of slip and the process of sliding in single asperity polymeric contacts. In this model, the peak tangential traction is capped by the shear strength, τ_0 of the contact interface, while the singularity in the traction distribution is eliminated. For a large Tabor (or Maugis) parameter, e.g. µ>5, Fig. S1(a) shows an initial peeling of the contact area (πa^2) due to the applied tangential force until the average slip displacement reaches the critical slip distance \bar{s}_0 , after which the contact area does not change. The additional work done by the external tangential force is dissipated through increased plasticity as the annulus of the slipped region (shaded in green) increases. When the far-field tangential force reaches the theoretical strength of the interface, $\pi a^2 \tau_0$, slip has penetrated to the center of the contact and the entire contact area has a uniform traction τ_0 . It is possible that at this point the contact can no longer dissipate any additional work done by the external force, and the entire contact begins to slide which is manifested as a pull-off or a displacement jump in a force-controlled experiment. This treatment shows that the interface slips after the entire contact area reaches a uniform shear stress that is equal to the shear strength of the interface, τ_0 . Equivalently, Fig. 4(d) shows that the interfacial shear stress does not depend on the problem length scale, i.e. the fiber diameter, and lies within a narrow band. These results provide a strong indication that the critical interfacial shear stress can be treated as a "material parameter" in the case of sliding of two polymer fibers interacting through strong van der Waals forces. Yet, the question arises whether τ_0 is related to the material shear strength, which is discussed in Section 3.2.3.

3.2.2. Prediction of contact area evolution with tangential force using a combined M-D and LEFM model

In the previous Section, it was shown that the modified JKR model predicted a consistent critical interfacial shear stress for the onset of sliding but did not predict the experimental instabilities. As mentioned in Section 3.1, the contact distance, z_0 , plays a key role in determining the regime of the proper contact adhesion model, i.e. JKR or M-D. According to the M-D model, a cohesive zone exists at the edge of the intimate contact over a central region of radius a, which eliminates the stress singularity. The cohesive zone with adhesive forces (or Dugdale stresses) of constant value σ_0 extends to a radius c, while in the annulus a < r < c, the surface separation increases monotonically from zero to a value h_0 , beyond which

the surfaces no longer interact with each other. The Maugis parameter, λ , in the M-D model, which is equivalent to Tabor's parameter ($\lambda=1.16\mu$), reflects the ratio of the elastic deformation to the deformation due to surface forces. For large values of λ (≥ 5), there is increased elastic deformation leading to a large central radius, a compared to the width of the annulus region, c-a, and the M-D model converges to the JKR model. It is, therefore, apparent that the M-D model provides a more versatile treatment of the contact adhesion problem for a much wider range of values for λ . When a tangential force is applied to the established contact, friction reduces the work of adhesion from w to w'=Xw and the Dugdale stress from σ_0 to $\sigma'_0=X\sigma_0$. Johnson (1997) re-derived the M-D model adding a tangential force term resulting in the following equations that are solved simultaneously to find the normalized contact radii, \bar{a} and \bar{c} (m=c/a), as a function of the normalized forces, \bar{P} . \bar{T} :

$$\frac{1}{2}\lambda\bar{a}^{2}\left\{\left(m^{2}-2\right)\cos^{-1}(1/m)+\sqrt{m^{2}-1}\right\}+\frac{4}{3}X\bar{a}\lambda^{2}\left\{\left(m^{2}-1\right)\cos^{-1}(1/m)-m+1\right\}=1\tag{18a}$$

$$\bar{P} = \bar{a}^3 - X\lambda \bar{a}^2 \left\{ m^2 \cos^{-1}(1/m) + \sqrt{m^2 - 1} \right\}$$
(18b)

$$X = 1 - \beta \frac{\bar{T}^2}{6\bar{a}^3} \tag{18c}$$

A typo in Eq. 4.8 of the original paper (Johnson, 1997) is corrected here. For large λ , $(c-a)/a = (m-1) \rightarrow 0$ and Eq. 18(b) reduces to Eq. 13(b), i.e. the JKR-LEFM case. The functional form of X, Eq. 18(c), was taken from the mode-mixity function adopted by Papangelo and Ciavarella, which facilitates the solution of Eq. 18(a,b).

For $\lambda = 0.98-1.57$ (for fiber diameters: 385-1595 nm, $z_0=1$ nm) Eq. 18(a,b) were solved. As an example, the contact area as a function of the tangential force for different values of β , is plotted in Fig. 5(a) for a 580-nm fiber and $\bar{P}=0$. For $\beta=1$, this modified M-D/LEFM model does predict the jump instability at ~200 nN, unlike the modified JKR model which was not able to predict the jump instability for this tangential force, Fig. 4(b). At the jump instability, the M-D/LEFM model predicts a ~30% reduction in the contact area. A similar reduction in the contact area was obtained for the other fiber diameters considered in this study. Fig. 5(b) shows the contact area reduction as a function of the tangential force for different normal forces and $\beta = 1$, similarly to Fig. 4(b). The initial M-D contact areas (M-D radius: b = a + 0.4(c - a) (Johnson, 1997)) gradually decrease until the tangential pull-off force is reached. The lower segments of the curves, though valid solutions to Eq. (18), cannot be realized in practice under force control, as in the present experiments. The square symbols represent the experimental tangential pull-off forces, which now correlate better with the predicted pull-off forces for small positive and negative values of the normal force. Compared to the combined JKR-LEFM model utilized in the previous section, the critical shear stresses, obtained from the experimental tangential pull-off force and the predicted contact area, are higher in the M-D/LEFM model because of the greater reduction in the contact area. Their values lie roughly on a straight line passing through the origin, thus averaging τ_0 =53±6 MPa for a 580-nm diameter fiber. For comparison, the steeper dashed line ($\tau_0 = 40$ MPa), also passing through the origin, represents the case of $\beta = 0$ (no change in the contact area with tangential force) as in Fig. 3(d). Note that the M-D/LEFM model predicts an increasing critical shear stress with increasing tangential force, as represented by the dashed red line which does not pass through the origin.

The aforementioned calculations for fibers with 585-nm diameter were expanded to other fiber diameters with a good correlation between the experimental and the predicted tangential pull-off force as a function of normalized normal force, Fig. 5(c). The M-D/LEFM model is able to predict some of the elastic jump instabilities observed in the experiments but for high values of β . The critical shear stress, τ_0 , calculated by dividing the mean experimental tangential pull-off forces by the estimated contact areas during pull-off, is approximately constant but with a larger variability than the prediction by the JKR-LEFM model, averaging τ_0 =52±8 MPa, Fig. 5(d). This critical shear stress, obtained through the M-D/LEFM model (which takes into account the reduction in contact area with tangential force) is 30% higher than the value of τ_0 = 40±4 MPa obtained via the M-D model that did not take into account the reduction in the contact area with the applied tangential force, Fig. 3(d).

Importantly, even if the experimental tangential pull-off force is larger than the theoretical prediction obtained for a particular value of β , e.g. P=-125 nN and $\beta=1$ in Fig. 5(b), the calculated critical shear stress does not change significantly if a different value of β (< 1) was used to obtain a better fit between the experiment and the model. This is because the contact area reduction at the tangential pull-off instability is almost identical for different values of $\beta \geq 0.4$ as shown in Fig. 5(a). Thus, the experimental tangential pull-off force divided by the reduced contact area obtained from the model would not change appreciably for that point. Fig. 5(c) shows that the theoretical tangential pull-off forces obtained for the 1595 nm fiber diameter and for $\beta=1$ are mostly lower than the experimental data. A lower value of $\beta=0.6$ provides a better fit with the experimental data, Fig. 5(c). However, the calculated shear strength was not substantially affected. Thus, the overall invariance of τ_0 to normal forces and fiber diameters, Fig. 5(d), gives support to the conclusion that τ_0 can be considered as a "material parameter".

Finally, the validity of using LEFM in Sections 3.2.1 and 3.2.2 to describe the experimental results must be examined. For $\lambda \ge 5$ (Section 3.2.1), the value of the ratio of the non-linear cohesive zone to the contact radius, (c-a)/a, is much smaller than unity, i.e. (c-a)/a <<1, therefore LEFM is valid. On the other hand, for $0.98 \le \lambda \le 2.06$ (Section 3.2.2), the value of (c-a)/a < 0.4. In this case, the non-linear zone is not much smaller than the contact size. Sills and Thouless (2015) used a non-dimensional fracture length-scale (defined as the ratio of the length of the process zone to the crack length) to assess

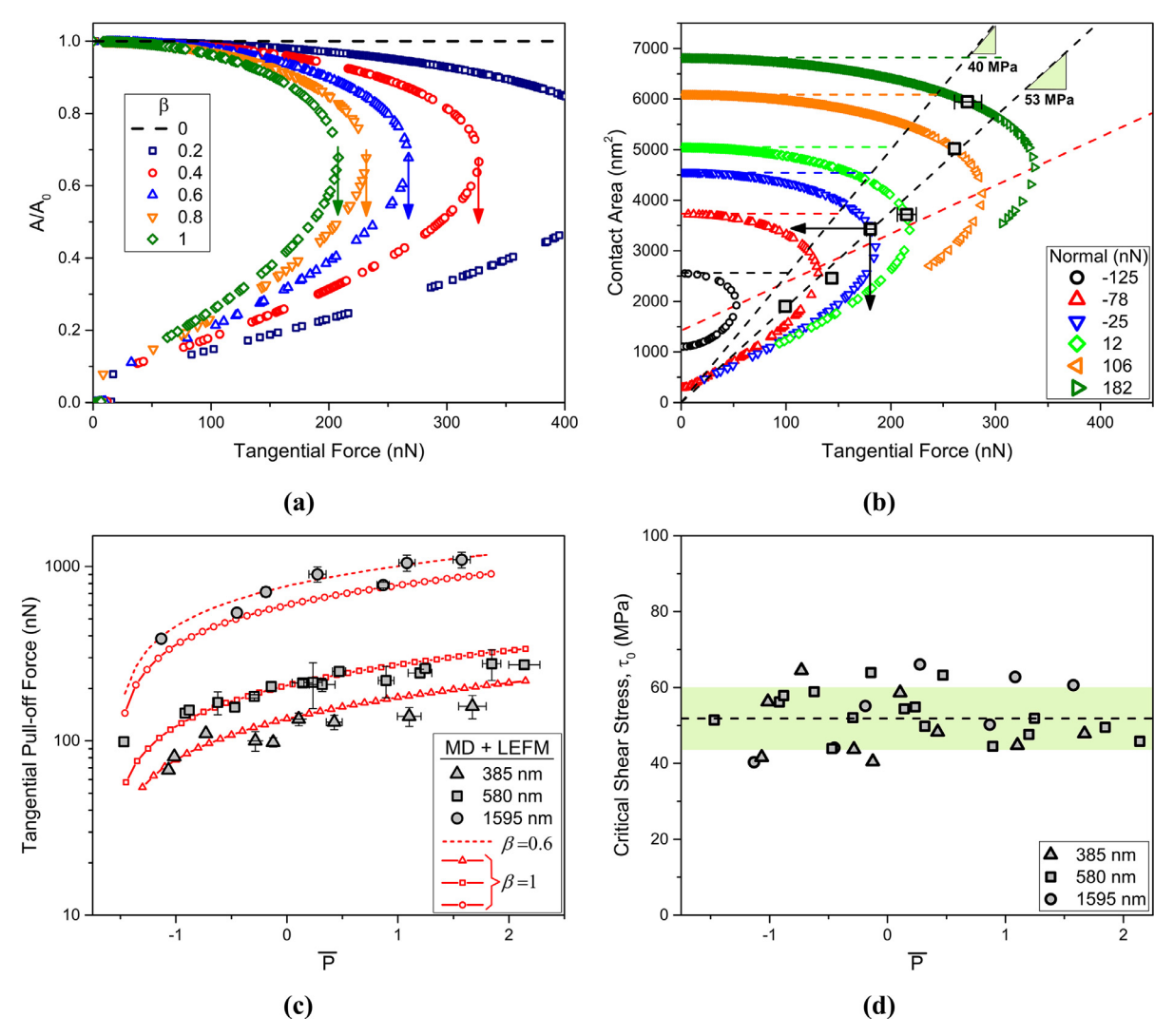


Fig. 5. (a) Effect of the non-dimensional parameter β on the contact area reduction for a 580-nm diameter fiber and $\bar{P}=0$, using the M-D/LEFM model. The contact area is normalized by the initial contact area before the tangential force is applied. The arrows point to the tangential force at the point of instability. (b) Reduction of the contact area with increasing tangential force for different values of the normal force and $\beta=1$. (c) Experimental vs. predicted tangential pull-off force for different fiber diameters and $\beta=1$. The case of $\beta=0.6$ provides the best fit only for the 1595 nm fiber. (d) Critical shear stress vs. normal force for different fiber diameters and $\beta=1$. The mean and the standard deviation are indicated by the dashed line and the green highlight, respectively. The average critical shear stress is 52 ± 8 MPa. (For interpretation of the references to colour in this figure legend, the reader is referred to the web version of this article.)

the validity of LEFM in such cases. It was shown that the ratio of the work done by the crack tip tractions to the nominal energy-release rate calculated through LEFM increases by only ~10% for a cohesive-length scale (c-a)/a = 0.4. Therefore, the use of LEFM to model the experimental results for (c-a)/a < 0.4 provides fairly accurate results.

3.2.3. Relationship between interfacial shear strength and shear yielding

Both methods of analysis pursued herein to extract the conditions for the onset of sliding between two crossing PAN nanofibers yielded a consistent value for the critical interfacial shear stress for all experimental conditions applied in this study, which points to a potential correlation between τ_0 and a material property. PAN is known to deform affinely to large strains, yet the specific mechanical properties depend on the processing conditions and the loading rate. Thus, uniaxial tension tests were performed on annealed PAN nanofibers at strain rates that were comparable to the shear strain rate applied to the fiber-fiber interface during the sliding experiments.

The elastic modulus value extracted from the stress-strain curves (3 GPa) was used in all calculations in this work. The 0.2% yield stress values extracted from typical stress-strain curves such as those in Fig. 6 were 70 MPa, 77 MPa, and 85 MPa for fibers with diameters 1805 nm, 620 nm, and 320 nm, respectively. The corresponding maximum shear stress values

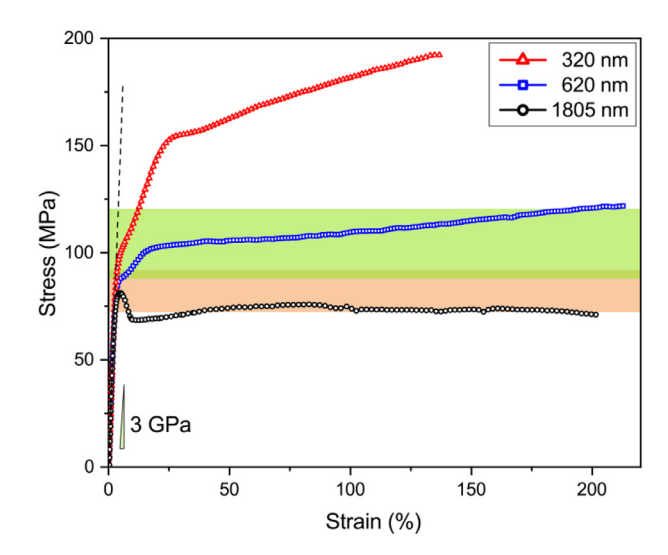


Fig. 6. Uniaxial stress-strain response of different diameter PAN fibers obtained at the strain rate of 8×10^{-4} s $^{-1}$. The orange and green highlights represent the normal stresses corresponding to the τ_0 predictions by the JKR-LEFM and M-D/LEFM models, respectively. (For interpretation of the references to colour in this figure legend, the reader is referred to the web version of this article.)

in the range of 35–43 MPa agree well with the value of τ_0 predicted by the JKR-LEFM model (41±5 MPa). On the other hand, tensile yielding occurred at ~100 MPa for the thinner fibers, corresponding to a maximum shear stress of 50 MPa that agrees well with the value of τ_0 predicted by the modified M-D/LEFM model (52±8 MPa). These correlations between the calculated critical shear stresses at the pull-off instability and the measured material properties from tensile tests indicate that shear yielding near the contact could be the controlling mechanism during shear detachment of PAN nanofibers that are characterized by strong van der Waals adhesion.

These results are consistent with the early work by Shooter and Tabor (1952) who showed that the frictional force between macroscale polymer surfaces (except polytetrafluoroethylene) was roughly equal to the product of the contact area with the bulk shear strength of the polymer. A similar relation was shown for metals (Bowden et al., 1943) in which the frictional force was comprised of two force contributions: the adhesion component of force (equal to the area of contact multiplied by the bulk shear strength of the softer metal) required to shear cold welded metallic junctions, and the ploughing or deformation component of the force required to displace the softer metal from the sliding path.

Furthermore, Briscoe (1986) identified two distinct regions where frictional dissipation may occur at the macroscale: an interface zone of ~100 nm, where the adhesion component dominates, and a subsurface zone (depth comparable to the contact length) where the deformation or ploughing component dominates. The processes occurring in the first region are considered to be independent of those occurring in the second region and vice versa. The adhesion component of the friction is generally described as the product of the area of contact and a shear stress or work parameter, τ , which can also be regarded as the rupture stress or the work for interfacial mode II fracture. Therefore, the better correlation between the yield properties of the thinner PAN fibers in Fig. 6 with the critical shear stress of the interface between two PAN nanofibers, $\tau_0 = 52 \pm 8$ MPa, could be because the effective mechanical properties of the thinner fibers provide a better representation of the surface properties that are relevant to the contact problem.

Hence, the results in this study indicate that the frictional force between nanoscale PAN fibers is equal to the product of the contact area and the shear stress for yielding a fiber surface layer. The significance of the interfacial shear strength in nanoscale contacts has received less attention. Carpick et al. (1996) reported the maximum shear strength of the contact between a Pt coated Si₃N₄ tip and mica to be 710 MPa or 910 MPa for the initial sliding of a blunt and a sharp tip, respectively. The shear yield strength of thin Pt films is 700–800 MPa (Das et al., 2016; Jonnalagadda et al., 2010) whereas the shear strength of mica can be as high as ~270 MPa (Properties and chemical composition of mica grade V1). Thus, the value of the shear strength obtained during the initial sliding corresponds to shearing of the Pt surface instead of the mica surface, which is unexpected since mica is softer. However, upon continuous sliding, the value of the shear strength gradually reaches 270 MPa, namely the shear strength of mica. Carpick et al. (1996) attributed the unconventional gradual decrease in shear strength to the gradual transfer/diffusion of potassium ions from the mica surface to the Pt tip during sliding. It should be noted that the shear strength determined from friction experiments is usually higher than that obtained from tension or shear tests, which may also be due to the increase in shear strength observed in most materials subjected to combined pressure-shear loading as in friction tests (Bowden et al., 1943). Additional explanations may be sought in the thin layer of the material near the interface, which could be stronger due to considerable amount of work hardening taking place in the area of contact.

4. Conclusions

This coupled experimental/theoretical investigation provided new quantitative insights into the open problem of sliding of individual soft (polymeric) nanofibers interacting through strong van der Waals forces. This problem is ubiquitous in networks of interconnected fibers/filaments in biological and bioengineered systems but has not been studied before for nanoscale fiber contacts. It is shown that for soft nanofibers interacting through strong van der Waals adhesion, the threshold shear stress for the onset of sliding and shear jump instabilities is constant and invariant of the contact radius, applied normal force, and nanofiber dimensions. This threshold stress is approximately equal to the shear yield stress of the polymer. Thus, shear yielding during sliding is identified as the origin of static friction in nanoscale soft contacts. The theoretical model employed herein, combining M-D elastic adhesive contact with LEFM, predicted the experimentally observed tangential pull-off force instabilities for different normal and shear force combinations, as opposed to the combined JKR-LEFM model that could not predict the experimentally observed instabilities. This study provides physical insights into the interaction between adhesion and friction at nanometer length scales. The results may impact the way we interpret the mechanics and energy dissipation in natural/artificial fibrous systems, with implications to the design of strong, resilient, and tough networks of soft nanofibers.

Declaration of Competing Interest

None.

CRediT authorship contribution statement

Debashish Das: Conceptualization, Methodology, Software, Validation, Formal analysis, Investigation, Writing - original draft, Writing - review & editing, Visualization. **Ioannis Chasiotis:** Conceptualization, Writing - review & editing, Supervision, Project administration, Funding acquisition, Data curation.

Acknowledgments

The authors acknowledge the support by the National Science Foundation via grant #1635681. The SEM studies were carried out at the Frederick Seitz Materials Research Laboratory Central Research Facilities, University of Illinois.

Supplementary material

Supplementary material associated with this article can be found, in the online version, at doi:10.1016/j.jmps.2020. 103931.

References

- Autumn, K., Liang, Y.A., Hsieh, S.T., Zesch, W., Chan, W.P., Kenny, T.W., Fearing, R., Full, R.J., 2000. Adhesive force of a single gecko foot-hair. Nature 405 (6787), 681.
- Bobaru, F., 2007. Influence of van der waals forces on increasing the strength and toughness in dynamic fracture of nanofibre networks: a peridynamic approach. Model. Simul. Mater. Sci. Eng. 15 (5), 397.
- Bowden, F.P., Moore, A.J.W., Tabor, D., 1943. The ploughing and adhesion of sliding metals. J. Appl. Phys. 14 (2), 80-91.
- Briscoe, B.J., 1986. Interfacial friction of polymer composites. In: General Fundamental principles. In Composite Materials Series, 1. Elsevier, pp. 25-59.
- Cao, H.C., Evans, A.G., 1989. An experimental study of the fracture resistance of bimaterial interfaces. Mech. Mater. 7 (4), 295–304.
- Carpick, R.W., Salmeron, M., 1997. Scratching the surface: fundamental investigations of tribology with atomic force microscopy. Chem. Rev. 97 (4), 1163–1194.
- Carpick, R.W., Agrait, N., Ogletree, D.F., Salmeron, M., 1996. Variation of the interfacial shear strength and adhesion of a nanometer sized contact. Langmuir 12, 3334–3340.
- Das, D., Power, B., Martin, J.P., Polcawich, R.G., Chasiotis, I., 2016. Role of oxide seed layer in plastic response of epitaxially grown textured metal films. Acta. Mater. 112, 390–402.
- Derjaguin, B.V., Muller, V.M., Toporov, Y.P., 1975. Effect of contact deformations on the adhesion of particles. J. Colloid Interface Sci. 53 (2), 314–326.
- Dietzel, D., Ritter, C., Mönninghoff, T., Fuchs, H., Schirmeisen, A., Schwarz, U.D., 2008. Frictional duality observed during nanoparticle sliding. Phys. Rev. Lett. 101 (12), 125505.
- Dong, Z., Kennedy, S.J., Wu, Y., 2011. Electrospinning materials for energy-related applications and devices. J. Power Sources 196 (11), 4886-4904.
- Feng, L., Li, S., Li, H., Zhai, J., Song, Y., Jiang, L., Zhu, D., 2002. Super-hydrophobic surface of aligned polyacrylonitrile nanofibers. Angew. Chem. Int. Ed. 41 (7), 1221–1223.
- Fuller, K.N.G., Tabor, D., 1975. The effect of surface roughness on the adhesion of elastic solids. Proc. R. Soc. Lond. A. Math. Phys. Sci. 345 (1642), 327–342. Guo, Y., Chang, Z., Guo, H.Y., Fang, W., Li, Q., Zhao, H.P., Feng, X.Q., Gao, H., 2018. Synergistic adhesion mechanisms of spider capture silk. J. R. Soc. Interface 15 (140), 20170894.
- Homola, A.M., Israelachvili, J.N., Gee, M.L., McGuiggan, P.M., 1989. Measurements of and relation between the adhesion and friction of two surfaces separated by molecularly thin liquid films. J. Tribol. 111 (4), 675–682.
- Homola, A.M., Israelachvili, J.N., McGuiggan, P.M., Gee, M.L., 1990. Fundamental experimental studies in tribology: the transition from "interfacial" friction of undamaged molecularly smooth surfaces to "normal" friction with wear. Wear 136 (1), 65–83.
- Hurtado, J.A., Kim, K.S., 1999. Scale effects in friction of single-asperity contacts. I. From concurrent slip to single-dislocation-assisted slip. Proc. R. Soc. Lond. Ser A: Math. Phys. Eng. Sci. 455 (1989), 3363–3384.
- Hutchinson, J.W., Suo, Z., 1991. Mixed mode cracking in layered materials. In: In Advances in Applied Mechanics, 29. Elsevier, pp. 63-191.
- Hutchinson, J.W., 1990. Mixed mode fracture mechanics of interfaces. Metal-Ceramic Interfaces 1990, 295-306.

Israelachvili, J.N., Tabor, D., 1972. The measurement of van der Waals dispersion forces in the range 1.5 to 130 nm. Proc. R. Soc. Lond. A. Math. Phys. Sci. 331 (1584), 19–38.

Israelachvili, J.N., 2011. Intermolecular and Surface Forces. Academic Press.

Johnson, K.L., Greenwood, J.A., 2005. An approximate JKR theory for elliptical contacts. J. Phys. D Appl. Phys. 38 (7), 1042.

Johnson, K.L., .Kendall K., and Roberts A.D. "Surface energy and the contact of elastic solids". In Proc. R. Soc. Lond. A, 324, no. 1558, pp. 301–313. The Royal Society, 1971.

Johnson, K.L., 1996. Continuum mechanics modeling of adhesion and friction. Langmuir 12 (19), 4510-4513.

Johnson, K.L., 1997. Adhesion and friction between a smooth elastic spherical asperity and a plane surface. Proc. R. Soc. Lond. A. Math. Phys. Sci. 453 (1956), 163–179.

Jonnalagadda, K.N., Chasiotis, I., Yagnamurthy, S., Lambros, J., Pulskamp, J., Polcawich, R., Dubey, M., 2010. Experimental investigation of strain rate dependence of nanocrystalline PT films. Exp. Mech. 50 (1), 25–35.

Li, L., Mangipudi, V.S., Tirrell, M., Pocius, A.V., 2001. Direct measurement of surface and interfacial energies of glassy polymers and pdms. In: Fundamentals of Tribology and Bridging the Gap Between the Macro-and Micro/Nanoscales. Springer, Dordrecht, pp. 305–329.

Liang, H.W., Wang, L., Chen, P.Y., Lin, H.T., Chen, L.F., He, D., Yu, S.H., 2010. Carbonaceous nanofiber membranes for selective filtration and separation of nanoparticles. Adv. Mater. 22 (42), 4691–4695.

Maeda, N., Chen, N., Tirrell, M., Israelachvili, J.N., 2002. Adhesion and friction mechanisms of polymer-on-polymer surfaces. Science 297 (5580), 379–382.

Maugis, D., 1992. Adhesion of spheres: the JKR-DMT transition using a Dugdale model. J. Colloid Interface Sci. 150 (1), 243–269.

Mergel, J.C., Sahli, R., Scheibert, J., Sauer, R.A., 2018. Continuum contact models for coupled adhesion and friction. J. Adhes. 1–33.

Naraghi, M., Chasiotis, I., Kahn, H., Wen, Y., Dzenis, Y., 2007a. Mechanical deformation and failure of electrospun polyacrylonitrile nanofibers as a function of strain rate. Appl. Phys. Lett. 91 (15), 151901.

Naraghi, M., Chasiotis, I., Kahn, H., Wen, Y., Dzenis, Y., 2007b. Novel method for mechanical characterization of polymeric nanofibers. Rev. Sci. Instrum. 78 (8), 085108.

Naraghi, M., Ozkan, T., Chasiotis, I., Hazra, S.S., De Boer, M.P., 2010. MEMS platform for on-chip nanomechanical experiments with strong and highly ductile nanofibers. J. Micromech. Microeng. 20 (12), 125022.

Naraghi, M., Arshad, S., Chasiotis, I., 2011. Molecular orientation and mechanical property size effects in electrospun polyacrylonitrile nanofibers. Polymer (Guildf) 52, 1612–1618.

Papangelo, A., Ciavarella, M., 2019. On mixed-mode fracture mechanics models for contact area reduction under shear load in soft materials. J. Mech. Phys. Solids 124, 159–171.

"Properties and chemical composition of mica grade V1Grade classification of muscovite mica". Properties and Chemical Composition of Mica Grade V1, https://www.tedpella.com/vacuum_html/Mica_Grade_V1_Properties.htm.

Picu, R.C., Sengab, A., 2018. Structural evolution and stability of non-crosslinked fiber networks with inter-fiber adhesion. Soft Matter 14 (12), 2254–2266. Pritykin, L.M., 1986. Calculation of the surface energy of homo-and copolymers from the cohesion parameters and refractometric characteristics of the respective monomers. J. Colloid Interface Sci. 112 (2), 539–543.

Qin, Z., Compton, B.G., Lewis, J.A., Buehler, M.J., 2015. Structural optimization of 3D-printed synthetic spider webs for high strength. Nat. Commun. 6, 7038. Ramakrishna, S., Fujihara, K., Teo, W.E., Yong, T., Ma, Z., Ramaseshan, R., 2006. Electrospun nanofibers: solving global issues. Mater. Today 9 (3), 40–50.

Rand, C.J., Crosby, A.J., 2006. Insight into the periodicity of Schallamach waves in soft material friction. Appl. Phys. Lett. 89 (26), 261907.

Sahli, R., Pallares, G., Ducottet, C., Ali, I.B., Al Akhrass, S., Guibert, M., Scheibert, J., 2018. Evolution of real contact area under shear and the value of static friction of soft materials. Proc. Natl. Acad. Sci. 115 (3), 471–476.

Savkoor, A.R., Briggs, G.A.D., 1977. The effect of tangential force on the contact of elastic solids in adhesion. Proc. R. Soc. Lond. A. Math. Phys. Sci. 356 (1684), 103–114.

Sengab, A., Picu, R.C., 2018. Filamentary structures that self-organize due to adhesion. Phys. Rev. E 97 (3), 032506.

Sheehan, P.E., Lieber, C.M., 1996. Nanotribology and nanofabrication of MOO3 structures by atomic force microscopy. Science 272 (5265), 1158-1161.

Shen, L., Glassmaker, N.J., Jagota, A., Hui, C.Y., 2008. Strongly enhanced static friction using a film-terminated fibrillar interface. Soft Matter 4 (3), 618–625. Shi, Q., Wan, K.T., Wong, S.C., Chen, P., Blackledge, T.A, 2010. Do electrospun polymer fibers stick? Langmuir 26 (17), 14188–14193.

Shi, Q., Wong, S.C., Ye, W., Hou, J., Zhao, J., Yin, J., 2012. Mechanism of adhesion between polymer fibers at nanoscale contacts. Langmuir 28 (10), 4663–4671. Shooter, K.V., Tabor, D., 1952. The frictional properties of plastics. Proc. Phys. Soc. London Sect. B 65 (9), 661.

Sills, R.B., Thouless, M.D., 2015. Cohesive-length scales for damage and toughening mechanisms. Int. J. Solids Struct. 55, 32–43.

Stachewicz, U., Hang, F., Barber, A.H., 2014. Adhesion anisotropy between contacting electrospun fibers. Langmuir 30 (23), 6819-6825.

Vader, D., Kabla, A., Weitz, D., Mahadevan, L., 2009. Strain-induced alignment in collagen gels. PLoS One 4 (6), e5902.

Vaenkatesan, V., Li, Z., Vellinga, W.P., de Jeu, W.H., 2006. Adhesion and friction behaviours of polydimethylsiloxane–A fresh perspective on JKR measurements. Polymer (Guildf) 47 (25), 8317–8325.

Varenberg, M., Peressadko, A., Gorb, S., Arzt, E., Mrotzek, S., 2006. Advanced testing of adhesion and friction with a microtribometer. Rev. Sci. Instrum. 77 (6), 066105.

Wang, M., Xu, D., Ravi-Chandar, K., Liechti, K.M., 2007. On the development of a mesoscale friction tester. Exp Mech 47 (1), 123-131.

Wang, X., Najem, J.F., Wong, S.C., Wan, Kai-tak, 2012. A nano-cheese-cutter to directly measure interfacial adhesion of freestanding nano-fibers. J. Appl. Phys. 111 (2), 024315.

Wang, X., Ding, B., Li, B., 2013. Biomimetic electrospun nanofibrous structures for tissue engineering. Mater. Today 16 (6), 229-241.

Wang, X., Wong, S.C., Jung, Y.J., Wan, K., 2017. Measuring interfacial adhesion of carbon nanotube bundles and electrospun polymer fibers. Langmuir 33 (44), 12592–12595.

Waters, J.F., Guduru, P.R., 2009. Mode-mixity-dependent adhesive contact of a sphere on a plane surface. Proc. R. Soc. Lond. A. Math. Phys. Sci. 466 (2117), 1303–1325.

Whitten, P.G., Brown, Hugh R., 2007. Polymer entanglement density and its influence on interfacial friction. Phys. Rev. E 76 (2), 026101.

Wu, S., 1982. Polymer Interface and Adhesion. Marcel Dekker, New York, NY, p. 187.

Xu, D., Liechti, K.M., Ravi-Chandar, K., 2007. On the modified tabor parameter for the JKR-DMT transition in the presence of a liquid meniscus. J. Colloid Interface Sci. 315 (2), 772–785.

Xu, D., Ravi-Chandar, K., Liechti, K.M., 2008. On scale dependence in friction: transition from intimate to monolayer-lubricated contact. J. Colloid Interface Sci. 318 (2), 507–519.